Vol. 11 • No. 19 • October 4 • 2023

www.advopticalmat.de

ADVANCED OPTICAL MATERIALS

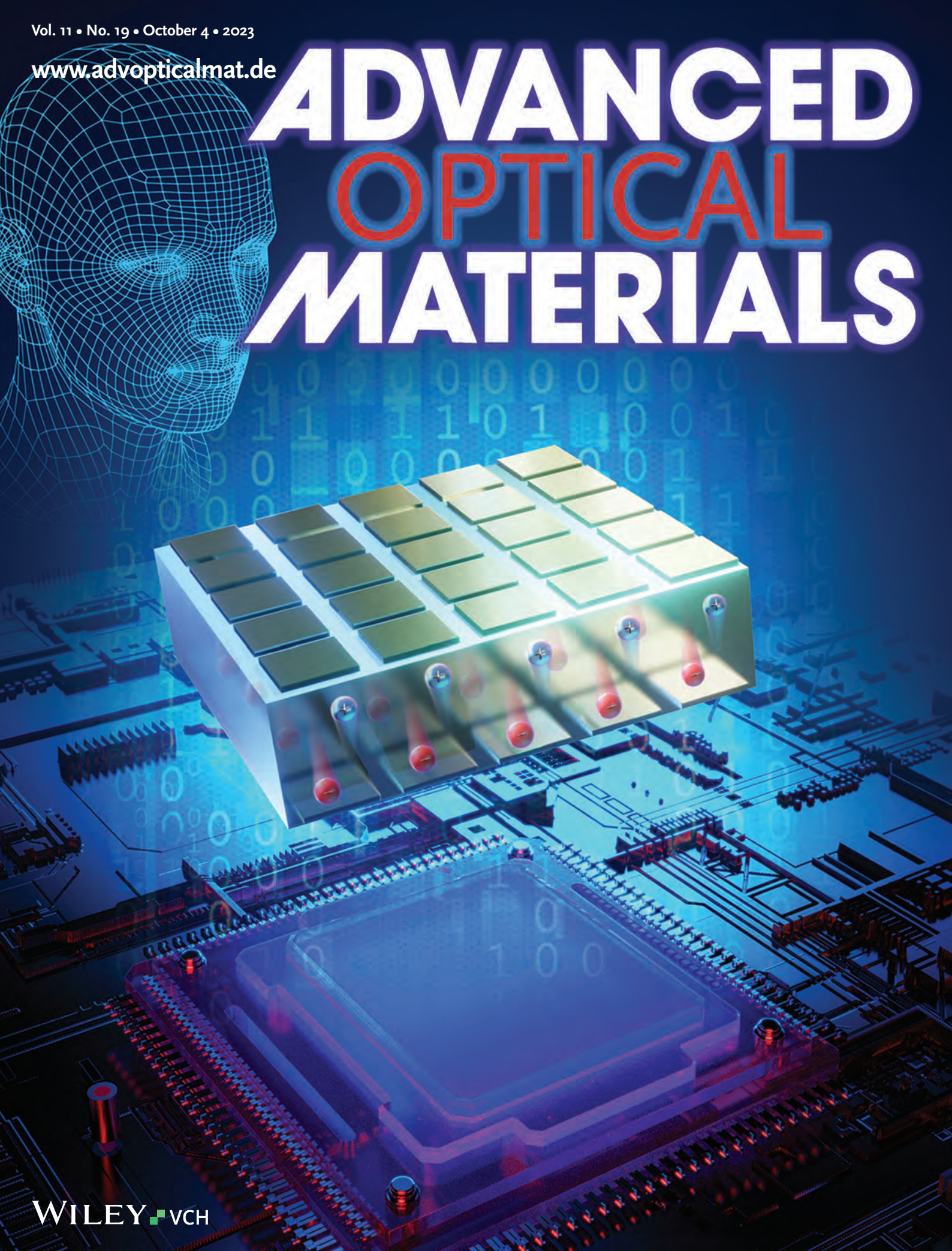

WILEY VCH

ADVANCED OPTICAL MATERIALS
www.advopticalmat.de

$Cs_3Cu_2I_5$ Single Crystal for Efficient Direct X-Ray Detection

Qinhua Wei, Xiongsheng Fan, Peng Xiang, Laishun Qin, Wenjun Liu, Tongyu Shi, Hang Yin, Peiqing Cai, Yufeng Tong, Gao Tang, Zugang Liu, Paul K. Chu, Hongsheng Shi,* Yanliang Liu,* and Xue-Feng Yu**

Low-dimensional copper-based halide single crystals are considered excellent scintillators for indirect X-ray detection, but their potential in direct X-ray detection has not been investigated. Herein, high-quality pure $Cs_3Cu_2I_5$ and Li-doped $Cs_3Cu_2I_5$:Li single crystals are grown by the Bridgman method. The Li^+ dopant enhances the photoelectric properties of the $Cs_3Cu_2I_5$ single crystal by extending the carrier lifetime, improving the carrier mobility from 6.49 to 9.52 $cm^2\ V^{-1}\ s^{-1}$, and increasing the mobility-lifetime ($\mu\tau$) product from 1.4×10^{-4} to 2.9×10^{-4} $cm^2\ V^{-1}$. The sensitive direct X-ray detector with a vertical device configuration of Au/$Cs_3Cu_2I_5$:Li single crystal/PCBM/Au is fabricated and demonstrated to have a high sensitivity of 831.1 $\mu C\ Gy_{air}^{-1}\ cm^{-2}$ and low detection limit of 34.8 $nGy_{air}\ s^{-1}$. Furthermore, the detector shows negligible baseline current drift and excellent stability upon X-ray radiation.

1. Introduction

X-ray imaging is widely used in medical diagnosis and treatment,[1] such as digital radiographic (DR)[2] and computerized tomography (CT).[3] However, a high radiation dose poses health and cancer hazards and so low-dose X-ray imaging is highly desirable. There are indirect and direct approaches in X-ray imaging.[4] The indirect converter with a typical sensitivity of 0.3 $\mu C\ Gy_{air}^{-1}\ cm^{-2}$ is more prevalent but suffers from low spatial resolution and quantum efficiency due to inevitable visible light scattering.[5] On the other hand, although the direct converter composed of semiconducting materials is able to monitor the X-ray excited charges[6] with higher sensitivity and spatial resolution in low-dose X-ray imaging, conventional semiconducting materials have some limitations and deficiencies. For instance, Si[7] and α-Se[8] lack sufficient stopping power for X-ray, consequently hindering operation in the high-energy range and HgI_2[9] detectors are plagued by the large leakage currents and low stability. CdZnTe[10] has shown great potential in room-temperature X-ray detection, there are drawbacks such as non-uniform charge transport and larger noise. In addition, the complicated preparation process and high fabrication cost pose practical challenges.[11]

Recently, halide perovskites possessing attractive properties, such as large radiation attenuation coefficients, high carrier mobility life product ($\mu\tau$), tunable bandgap and volume resistivity, and high fluorescence yields,[12,13] have been proposed to be efficient direct X-ray irradiation detectors.[14] However, common lead halide organic-inorganic perovskites suffer from the poor environmental stability and toxicity of lead-based salts,[15,16] Lead-free copper-based halides show large radiation attenuation, high photoluminescence quantum yield (PLQY), lack of self-absorption, and good air-stability,[17–19] rendering it suitable for X-ray imaging and γ-ray detection, especially the 0D $Cs_3Cu_2I_5$ crystal. For example, clear reconstructed 3D snail CT images have been obtained by the $Cs_3Cu_2I_5$ nanocrystal-based fiber-optic panel.[20] The $Cs_3Cu_2I_5$:Tl single crystal simultaneously exhibits high scintillation yield and remarkable energy resolution under ^{137}Cs γ-ray radiation in conjunction with low detection limit and afterglow in indirect X-ray detection.[21,22] The Li^+-doped $Cs_3Cu_2I_5$ single crystal also has an excellent figure-of-merit, which can be used in the field of dual gamma-ray and neutron detection.[23] Moreover, the $Cs_3Cu_2I_5$:In single crystal-based

Q. Wei, P. Xiang, L. Qin, H. Yin, Y. Tong, G. Tang
College of Materials and Chemistry
China Jiliang University
Hangzhou 310018, China
E-mail: qinlaishun@cjlu.edu.cn
X. Fan, W. Liu, T. Shi, Y. Liu, X.-F. Yu
Materials Interfaces Center
Shenzhen Institute of Advanced Technology
Chinese Academy of Sciences
Shenzhen, Guangdong 518055, China
E-mail: yl.liu4@siat.ac.cn; xf.yu@siat.ac.cn
X. Fan, P. Cai, Z. Liu
College of Optical and Electronic Technology
China Jiliang University
Hangzhou 310018, China
H. Yin
State Key Laboratory of Molecular Reaction Dynamics
Dalian Institute of Chemical Physics
Chinese Academy of Science
Dalian 116023, China
P. K. Chu
Department of Physics
Department of Materials Science and Engineering
and Department of Biomedical Engineering
City University of Hong Kong
Tat Chee Avenue, Kowloon, Hong Kong 999077, China
H. Shi
Xinjiang Technical Institute of Physics and Chemistry
Chinese Academy of Sciences
Urumqi 830011, China
E-mail: shihs@ms.xjb.ac.cn

The ORCID identification number(s) for the author(s) of this article can be found under https://doi.org/10.1002/adom.202300247

DOI: 10.1002/adom.202300247

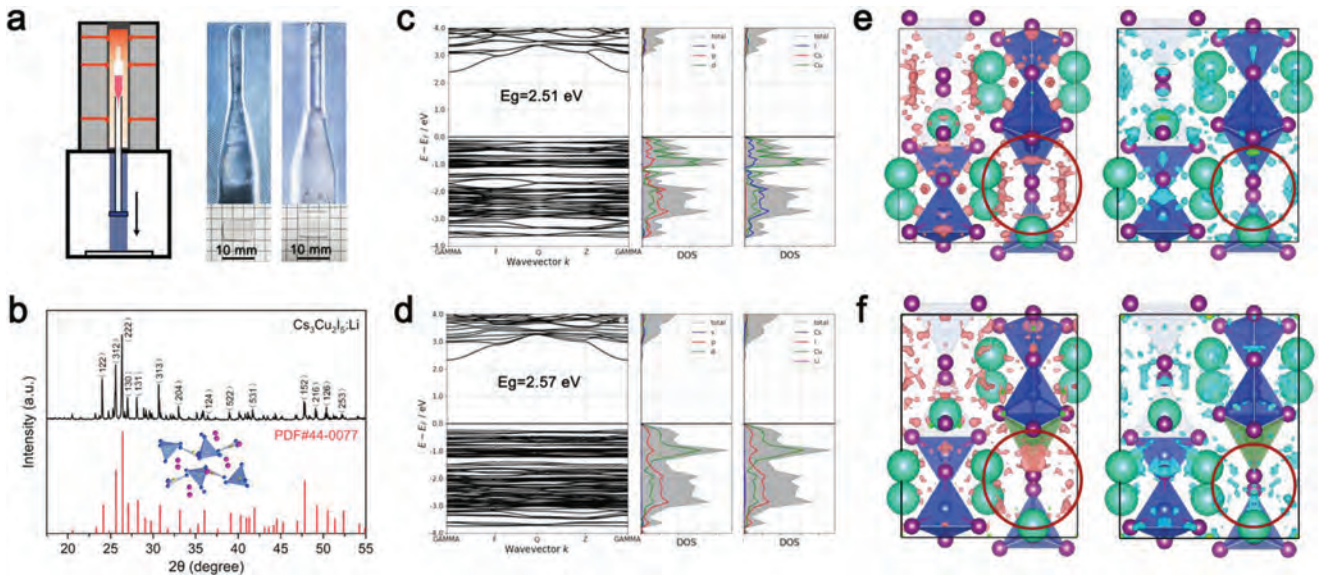

Figure 1. a) Schematic diagram of the vertical Bridgman furnace for crystal growth and photographs of the as-grown $Cs_3Cu_2I_5$ and $Cs_3Cu_2I_5$:Li single crystals and machined samples. b) Powder XRD pattern of $Cs_3Cu_2I_5$:Li. Electronic band structure of c) pure and d) Li^+-doped $Cs_3Cu_2I_5$. Charge density maps of VBM and CBM of e) pure and f) Li^+-doped $Cs_3Cu_2I_5$.

imaging system has excellent spatial resolution.[24] Because of the $Cs_3Cu_2I_5$ is constructed with $[Cu_2I_5]^{3-}$ coordinated polyhedron, spatially separated by Cs^+ that only serves as a skeleton to form the localized electronic structure.[25] The beneficial disrupted ion migration channels avoid the dark current noise and baseline drift problems at high bias voltages,[26] thereby maintaining the resolution and stability of the $Cs_3Cu_2I_5$-based detector. In direct X-ray detection by the $Cs_3Cu_2I_5$ single crystal, the semiconductor converts X-ray into electrical signals with high sensitivity and spatial resolution. In the previous report, the Li^+ doping was found able to reduce the shallow defects, boosting the carrier lifetime of the $Cs_3Cu_2I_5$ single crystal,[27] which is benefit for direct X-ray detection. In addition, the radius of Li^+ (0.59 Å) is close Cu^+ (0.60 Å) and the Li^+ can partly replace the Cu^+ in $Cs_3Cu_2I_5$ single crystal.

In this work, the strategy of Li^+-doped was adopted to enhance the photoelectric properties of $Cs_3Cu_2I_5$ single crystal by extending the carrier lifetime and improving the carrier mobility. The pure $Cs_3Cu_2I_5$ and Li-doped $Cs_3Cu_2I_5$:Li single crystals with a diameter of 12 mm are prepared by the Bridgman method and their properties pertaining to direct X-ray detection are investigated. The pure $Cs_3Cu_2I_5$ single crystal has moderate electronic properties such as carrier mobility of 6.49 $cm^2\ V^{-1}\ s^{-1}$ and mobility-lifetime ($\mu\tau$) product of $1.4 \times 10^{-4}\ cm^2\ V^{-1}$. Doping with lithium improves optical–electrical properties including bigger carrier mobility of 9.52 $cm^2\ V^{-1}\ s^{-1}$ and mobility-lifetime ($\mu\tau$) product of $2.9 \times 10^{-4}\ cm^2\ V^{-1}$. Subsequently, the direct X-ray detector assembled with the $Cs_3Cu_2I_5$:Li single crystal shows a high sensitivity of 831.1 $\mu C\ Gy_{air}^{-1}\ cm^{-2}$ and low detection limit of 34.8 $nGy_{air}\ s^{-1}$. The detector also exhibits excellent stability with negligible current drifts during continuous X-ray exposure.

2. Results and Discussion

2.1. Crystal Growth and First-Principle Calculation

Figure 1a presents the schematic diagram of the custom vertical Bridgman growth furnace with three zones. The temperature gradient can be adjusted from 10 to 25 °C for a length of 40 mm and the descending speed can be adjusted up to 0.001 mm h^{-1}. The pure $Cs_3Cu_2I_5$ and 2.5 at% Li^+-doped $Cs_3Cu_2I_5$:Li single crystals are grown by the self-seeding Bridgman technique with a capillary tube. The as-grown $Cs_3Cu_2I_5$:Li single crystal ingots with a diameter of 12 mm and transparent machined sample without cracks and visible inclusions are exhibited in Figure 1a. The Inductively coupled plasma optical emission spectrometry (ICP-OES) result shows that the mass percentage of Li^+ in $Cs_3Cu_2I_5$:Li crystal is 0.0011%, and the atomic percentage relative to Cu^+ was calculated to be 0.92 at.%, indicating that the Li^+ was introduced successfully. But the segregation coefficient of Li^+ is lower than one. Therefore, the distribution of Li^+ is nonuniformity and enriched in the bottom as crystal grown, which indicates that the high concentration doping of Li^+ is difficult for the $Cs_3Cu_2I_5$ host. The powder XRD pattern of the polycrystalline $Cs_3Cu_2I_5$:Li can be indexed to the pure $Cs_3Cu_2I_5$ PDF card #45-0077 revealing the absence of impurity phases like CsI or CuI, as shown in Figure 1b. $Cs_3Cu_2I_5$ crystallizes into the orthorhombic space group of Pnma at room temperature. Consider for the radius of Li^+ (0.59 Å) is closer to that of Cu^+ (0.60 Å), the Li^+ exhibits a tendency to substitute for the Cu^+ site.

To gain mechanistic insights into the optical properties of the Li^+ doped effect on $Cs_3Cu_2I_5$ single crystals, the electronic band structures are derived by density-functional theory (DFT) calculation with the PBE hybrid functional. Both the valence band

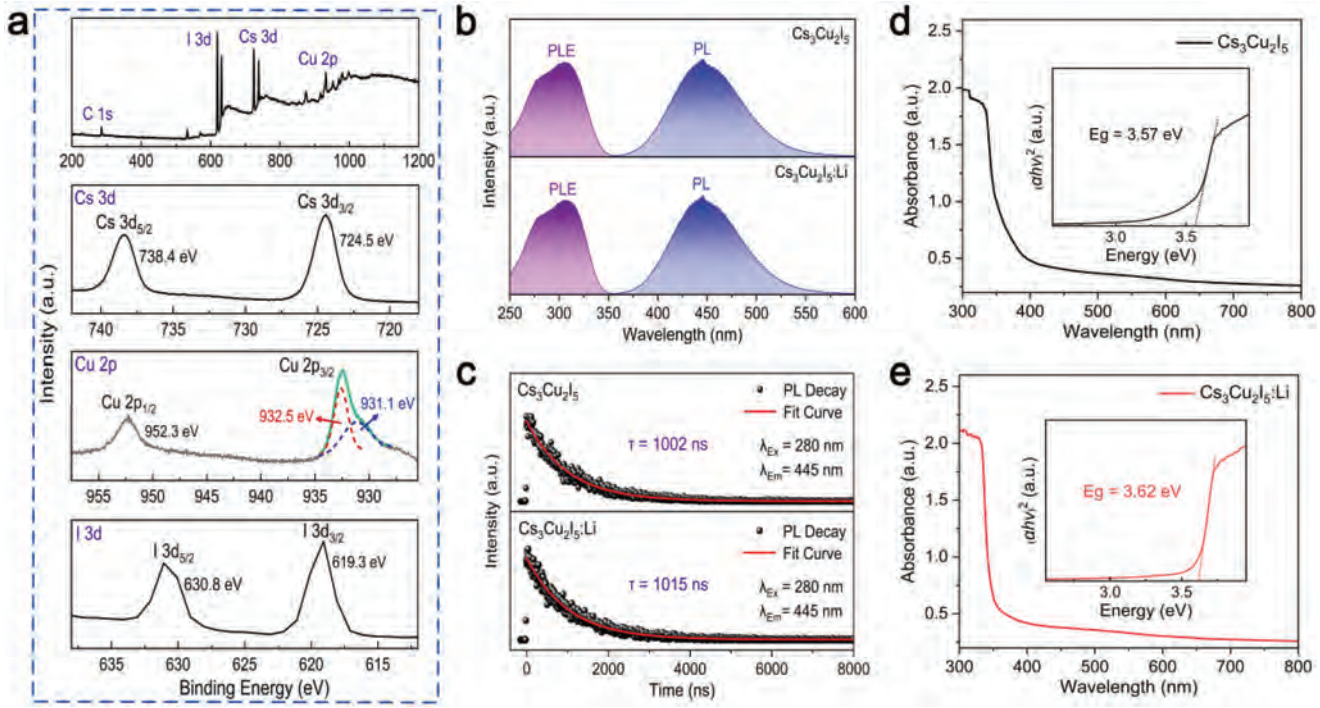

Figure 2. a) XPS survey spectrum of $Cs_3Cu_2I_5$:Li and High-resolution XPS spectra of Cs 3d, Cu 2p and I 3d. b) Photoluminescence emission and excitation spectra and c) Decay profiles of pure and Li^+-doped $Cs_3Cu_2I_5$. Absorption spectra of d) pure and e) Li^+-doped $Cs_3Cu_2I_5$ (Inset: Tauc plot showing the direct bandgap).

edges in Figure 1c,d are completely flat between the *F* and *Z* direction, which differ from the large bandwidth and dispersion band edges of conventional 3D structures. The direct bandgap of $Cs_3Cu_2I_5$ is smaller than that of Li^+-doped $Cs_3Cu_2I_5$, indicating a broken symmetry after introducing Li^+ to enlarge the bandgap. The calculated absolute value of E_g deviates from the experiment data, results from the nature of Perdew–Burke–Ernzerhof (PBE) method.[28] According to the total density of states (DOS) and projected DOS (PDOS) map, the valence band maximum (VBM) is mainly contributed by the I-p orbitals and some Cu-d orbitals. Whereas, the conduction band minimum (CBM) density states are mainly composed of Cu-4s and I-5p orbitals. The flat VBM energy profiles of pure and Li^+-doped $Cs_3Cu_2I_5$ indicate localized charge distributions corresponding to the charge density maps of VBM and CBM (Figure 1e,f). In particular, most of the charges of Li^+-doped $Cs_3Cu_2I_5$ transfer from the $[LiI_6]$ octahedrons to $[CuI_6]$ octahedrons while some charges transfer from the metal to halide upon photoexcitation from VBM to CBM as shown in Figure 1f marked with red circle. Compared to the pure $Cs_3Cu_2I_5$, more prominent charge transfer in Li^+-doped $Cs_3Cu_2I_5$ enhances the conductivity and doping with Li extends the carrier lifetime and improves the carrier mobility.

2.2. Optical Properties of Pure and Li^+-Doped $Cs_3Cu_2I_5$ Single Crystal

The survey X-ray photoelectron spectroscopy (XPS) spectrum of $Cs_3Cu_2I_5$:Li crystal in **Figure 2**a reveals the C 1s, Cs 3d, Cu 2p, and I 3d components and the high-resolution spectra are conducted to validate the chemical states of matrix ions. The binding energies of Cu $2p_{1/2}$ and Cu $2p_{3/2}$ are consistent with Cu–I bond and demonstrate the presence of Cu^+ in the host. The satellite peak for the Cu^{2+} oxidation state cannot be observed. The binding energies of the 3d orbital correspond to the Cs and I +1 and −1 states, respectively. Compared to the XPS result of $Cs_3Cu_2I_5$ crystal, presenting in Figure S1 (Supporting Information), the Li^+ doped has no influence on chemical states of the crystal composition, except that the peaks position has a slight shift of 0.4 eV. The The photoluminescence excitation (PLE) and photoluminescence (PL) spectra of pure $Cs_3Cu_2I_5$ and $Cs_3Cu_2I_5$:Li single crystals was measured and shown in Figure 2b while the time resolved PL decay time curves were shown in Figure 2c. After Li^+ doping, the excitation (at 310 nm) and emission (at 445 nm) bands do not show obvious changes, but the decay time becomes slightly longer from 1002 to 1015 ns, indicating that the Li^+-doped $Cs_3Cu_2I_5$ crystal has a longer electron–hole recombination time. Hence, the mobility-lifetime (μτ) product increases with Li^+ doping boding well for direct X-ray detection. Figure 2d,e presents the ultraviolet–visible absorption spectra of the pure and Li^+-doped $Cs_3Cu_2I_5$ sample, respectively. The inset is the Tauc plot curve converted by the Kubelka–Munk equation for the bandgap calculation.[29] Both the pure and Li^+-doped $Cs_3Cu_2I_5$ exhibit a sharp absorption edge indicative of a direct bandgap. The corresponding bandgap energy (E_g) of $Cs_3Cu_2I_5$:Li is estimated to be 3.62 eV, which is bigger than that of the pure $Cs_3Cu_2I_5$ crystal (3.57 eV) and slightly exceeds that of the conventional semiconductor X-ray detector.[30] This trend is in good agreement with the DFT calculation shown in Figure 1c,d.

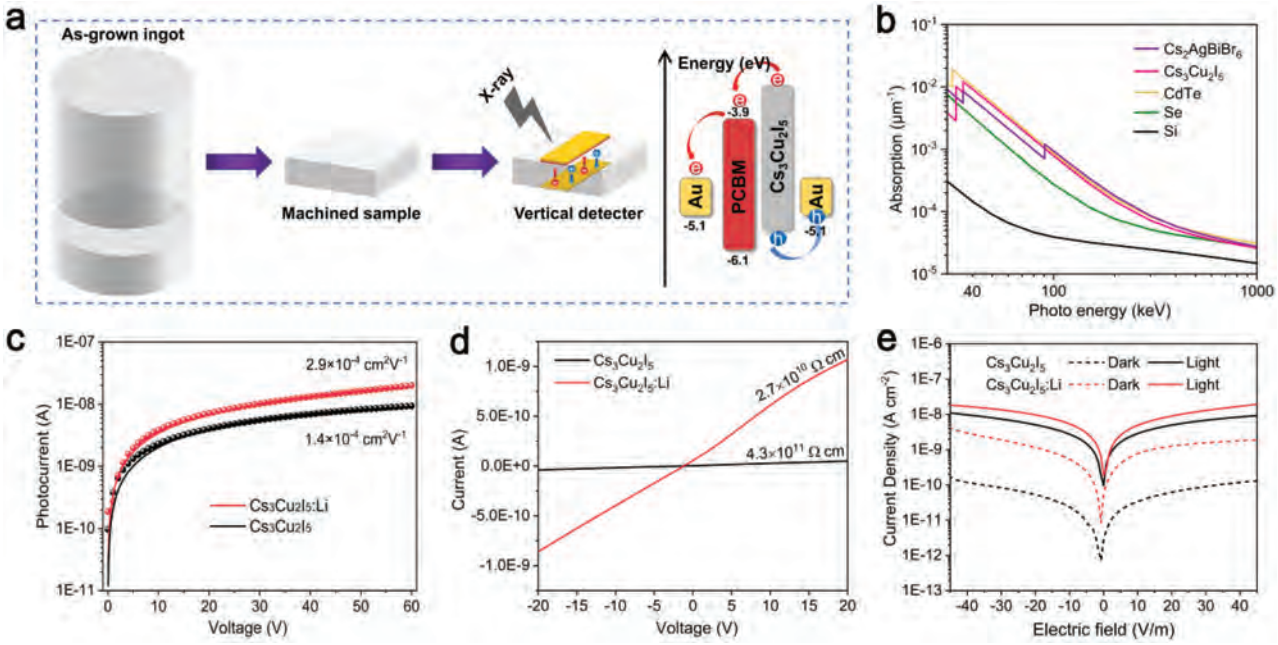

Figure 3. a) Schematic of X-ray detector fabrication and device configuration, Calculated attenuation coefficient of various semiconductors for different X-ray b) energy, c) Photoconductivity, d) resistivity spectra of the $Cs_3Cu_2I_5$ and $Cs_3Cu_2I_5$:Li. e) *J–V* characteristics of the $Cs_3Cu_2I_5$ and $Cs_3Cu_2I_5$:Li assisted X-ray detectors.

2.3. Electronic Properties of the $Cs_3Cu_2I_5$ Single Crystal

The DC field Hall effect of the machined samples was measured using the van der Pauw method to investigate the electronic properties. Au evaporated on the four corners was used as the electrodes. The excitation current was 0.1 mA, and the excitation magnetic field was 0.5 T. The results present that the two samples exhibit *n*-type conductivity. The $Cs_3Cu_2I_5$:Li single crystal has higher carrier mobility of 9.52 $cm^2\ V^{-1}\ s^{-1}$ than the pure $Cs_3Cu_2I_5$ single crystal (6.49 $cm^2\ V^{-1}\ s^{-1}$), and it is larger than that of $Cs_3Bi_2Br_9$ (1.54 $cm^2\ V^{-1}\ s^{-1}$)[31] and two times that of $Cs_2AgBiBr_6$ (3.17 $cm^2\ V^{-1}\ s^{-1}$)[32] and $MAPbBr_3$ (4.16 $cm^2\ V^{-1}\ s^{-1}$).[33] It means that the Li dopant enhances the conductivity of the $Cs_3Cu_2I_5$ single crystal, and the positive effect on the conductivity is confirmed by experiments and DFT calculation.

The pure $Cs_3Cu_2I_5$ and $Cs_3Cu_2I_5$:Li single crystal ingots are machined into squares and integrated into X-ray detectors with the stacked structure of Au/$Cs_3Cu_2I_5$ or $Cs_3Cu_2I_5$:Li/PCBM/Au and level alignment as shown in **Figure 3**a. The PCBM is an electron transport layer, which is able to reduce the potential barrier between the crystal interface and the metal electrode. Figure 3b compares the absorption coefficients of typical and potential materials for X-ray detection, which were calculated according to the photon cross-section database.[34] Since $Cs_3Cu_2I_5$ consisting of heave elements of Cs, Cu, and *I* have a large high density (4.52 g cm^{-3}), it has a bigger X-ray absorption coefficient than $Cs_2AgBiBr_6$, *α*-Se, and commercial silicon, and comparable with CdTe. The photoconductivity measurements are carried out to determine the optoelectronic properties of the $Cs_3Cu_2I_5$ and $Cs_3Cu_2I_5$:Li single crystal, as shown in Figure 3c. The photocurrent response is monitored by applying a voltage ranging from 0 to 60 V and the Hecht formula is employed to fit the photocurrent–voltage curve:

$$I = I_0 \mu\tau V/L^2 \left(1 - exp\left(-L^2/\mu\tau V\right)\right) \quad (1)$$

where I_0 is the saturated current, L is the thickness of the $Cs_3Cu_2I_5$ and $Cs_3Cu_2I_5$:Li single crystal, and V is the applied voltage. The $\mu\tau$ products of the pure $Cs_3Cu_2I_5$ and $Cs_3Cu_2I_5$:Li single crystal are determined to be 1.4×10^{-4} and 2.9×10^{-4} $cm^2\ V^{-1}$, respectively, and the bigger $\mu\tau$ product indicates enhanced transport of photogenerated charges. Moreover, the $Cs_3Cu_2I_5$:Li single crystal has a smaller resistivity of 2.7×10^{10} Ω cm compared to 4.3×10^{11} Ω cm of the $Cs_3Cu_2I_5$ single crystal, as shown in Figure 3d,e shows the current density–voltage (*J–V*) characteristics of the X-ray detectors made of the $Cs_3Cu_2I_5$ and $Cs_3Cu_2I_5$:Li single crystals. The $Cs_3Cu_2I_5$ X-ray detector exhibits obviously lower dark currents than $Cs_3Cu_2I_5$:Li due to the high resistivity, and the dark current mainly comes from the injected current form the electrodes at the applied electric field. Meanwhile, the $Cs_3Cu_2I_5$:Li X-ray detector shows a significantly enhanced light current of 2.0×10^{-8} A cm^{-2} at an electric field of 45 V mm^{-1}, which is more than twice that of the $Cs_3Cu_2I_5$ X-ray detector of 9.3×10^{-9} A cm^{-2}. The light current originates from the X-ray excited photocurrent, and the Li-doped $Cs_3Cu_2I_5$:Li single crystal possesses higher conductivity due to enhanced charge transport thus facilitating high-sensitivity X-ray detection.

2.4. Direct X-Ray Detection

To obtain dynamic information from the $Cs_3Cu_2I_5$ and $Cs_3Cu_2I_5$:Li X-ray detectors, the time-resolved light current

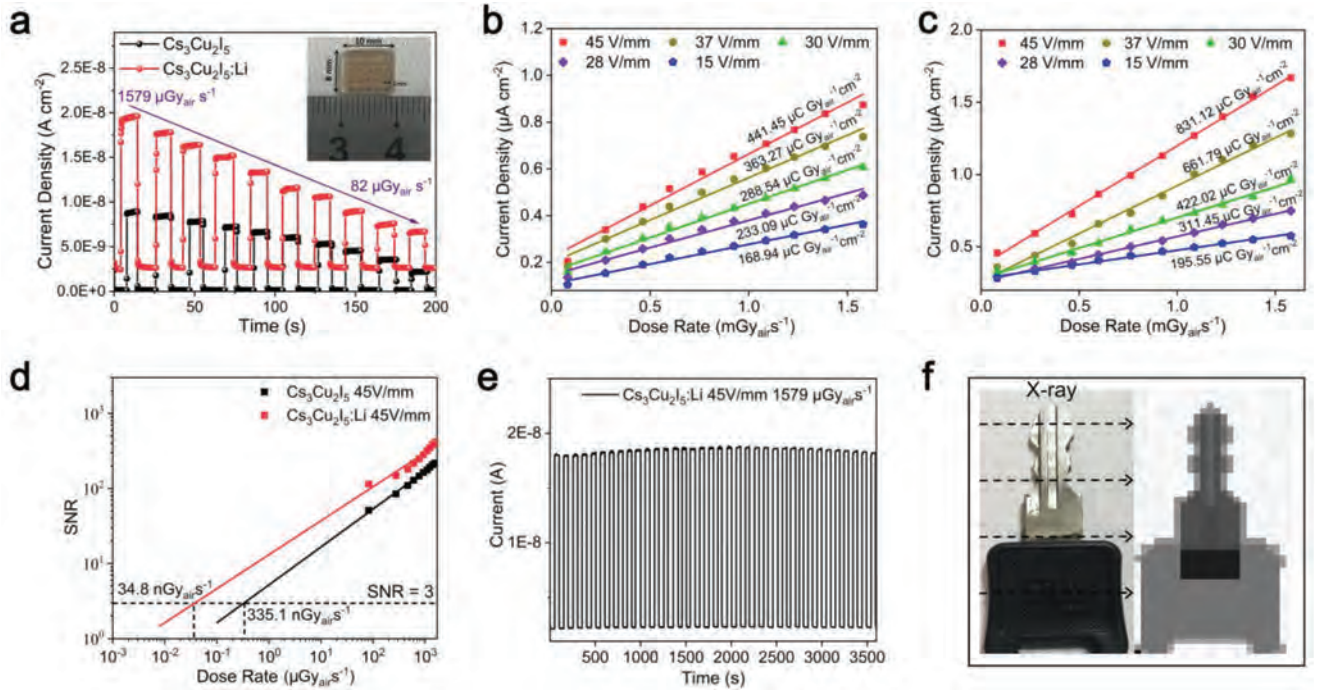

Figure 4. a) X-ray response of the $Cs_3Cu_2I_5$ and $Cs_3Cu_2I_5$:Li assisted X-ray detectors and the picture of detector. Current densities generated by X-ray as a function of dose rates at different applied electrical fields for b) $Cs_3Cu_2I_5$ and c) $Cs_3Cu_2I_5$:Li detectors. d) Dose rate dependent SNR of the detectors. e) Stability of the $Cs_3Cu_2I_5$:Li detector under pulsed X-ray irradiation at a fixed dose rate. f) Optical and X-ray images of a metallic key.

response for various X-ray dose rates from 1579 to 82 μGy$_{air}$ s^{-1} are presented in **Figure 4**a, the inset is the picture of detector. The sizes of the single X-ray detector and the array are 1 mm × 1 mm and 8 mm × 10 mm, respectively. Both detectors show decent response signals upon on/off X-ray switching and good linear relationship with the X-ray dose rates. The $Cs_3Cu_2I_5$:Li X-ray detector exhibits obviously higher dark currents and light currents with larger X-ray on–off than the pure $Cs_3Cu_2I_5$ detector at an electric field of 45 V mm^{-1}, indicating the $Cs_3Cu_2I_5$:Li X-ray detector has more sensitive X-ray detection properties. Figure S2 (Supporting Information) presents the current response of the $Cs_3Cu_2I_5$ and $Cs_3Cu_2I_5$:Li detectors during X-ray on/off at different electric fields and X-ray dose rates.

To investigate the sensitivity of the $Cs_3Cu_2I_5$ and $Cs_3Cu_2I_5$:Li X-ray detectors, the X-ray generated photocurrent density are plotted as a function of X-ray dose rates as shown in Figure 4b,c. The sensitivity of the X-ray detector can be calculated from the slope of the photocurrents versus X-ray dose rates plots acquired at different electric fields. The pure $Cs_3Cu_2I_5$ detector has X-ray sensitivities of 441.5, 363.3, 288.5, 233.1, and 168.9 μC Gy$_{air}^{-1}$ cm^{-2} at 45, 37, 30, 28, and 15 V mm^{-1}, respectively. In comparison, the $Cs_3Cu_2I_5$:Li X-ray detector shows enhanced sensitivities of 831.1, 661.8, 422.0, 311.5, and 95.6 μC Gy$_{air}^{-1}$ cm^{-2} at electric fields of 45, 37, 30, 28, and 15 V mm^{-1}, respectively.

The signal-to-noise ratio (SNR) is another important parameter for X-ray detection and can be calculated by the following equation:

$$SNR = I_{signal}/I_{noise} = \left(I_{photo} - I_{dark}\right)/I_{noise} \quad (2)$$

where I_{photo} is the average current during X-ray irradiation, I_{dark} is the average dark current derived from parallel experiments at each bias, and I_{noise} is the noise current calculated from the standard deviation of the photocurrents. The SNRs of the X-ray detectors at an electric field of 45 V mm^{-1} are plotted as a function of dose rates in Figure 4d. The limit-of-detection (LoD) was linearly extrapolated from the X-ray dose rate dependent SNR following the International Union of Pure and Applied Chemistry standard with a SNR value of three. The $Cs_3Cu_2I_5$:Li X-ray detector has a smaller LoD of 34.8 nGy$_{air}$ s^{-1} than the pure $Cs_3Cu_2I_5$ X-ray detector of 335.1 nGy$_{air}$ s^{-1}, which is consistent with the higher sensitivity of the $Cs_3Cu_2I_5$:Li X-ray detector. Then, we highlight the performance of perovskite-based X-ray direct conversion detectors and summarize the important parameters including the μτ product, sensitivity, detection limit and resistivity in Table S1 (Supporting Information). The $Cs_3Cu_2I_5$:Li crystal presents good comprehensive performance.

To evaluate the detection stability under continuous operating conditions, X-ray on/off experiments are carried out at the 45 V mm^{-1} external electric field and 1579 μGy$_{air}$ s^{-1} X-ray dose for 3600 s as shown in Figure 4e and Figure S3 (Supporting Information). Both the $Cs_3Cu_2I_5$ and $Cs_3Cu_2I_5$:Li X-ray detectors exhibit reproducible and stable response with small X-ray on/off changes, indicating excellent materials and working stability under continuous X-ray exposure. The temporal baseline tracking of the X-ray detectors shown in Figure S4 (Supporting Information), and the current drift (I_{drift}) can be calculated by the following equation:

$$I_{drift} = \left(I_t - I_0\right)/\left(E \times S \times t\right) \quad (3)$$

where I_t is the current at time t, I_0 is the current immediately after stabilization, E is the electric field, and S is the area of the device. Both the $Cs_3Cu_2I_5$ and $Cs_3Cu_2I_5$:Li X-ray detectors are able to maintain stable dark and light currents in 3600 s, and both of the $Cs_3Cu_2I_5$ and $Cs_3Cu_2I_5$:Li X-ray detectors show smaller light current drifts of 1.17×10^{-4} and 1.35×10^{-4} A cm^{-1} s^{-1} V^{-1}, indicating excellent working stability.

The X-ray imaging capability of the $Cs_3Cu_2I_5$:Li X-ray detector is assessed by x–y scanning experiments with a key containing a plastic handle and metal bit as the imaging target. As shown in Figure 4f, the X-ray image clearly reveals a clear outline of the key consistent with the optical image in the scanning mode.

3. Conclusion

The pure $Cs_3Cu_2I_5$ and Li^+-doped $Cs_3Cu_2I_5$:Li single crystals are studied for high sensitivity direct X-ray detection. The high quality pure $Cs_3Cu_2I_5$ single crystal with a size of 12 mm is grown by the Bridgman method, and doped with Li^+ to form $Cs_3Cu_2I_5$:Li single crystal. The pure $Cs_3Cu_2I_5$ single crystal shows moderate electronic properties with carrier mobility of 6.49 cm^2 V^{-1} s^{-1} and mobility-lifetime ($\mu\tau$) product of 1.4×10^{-4} cm^2 V^{-1}. In comparison, the $Cs_3Cu_2I_5$:Li single crystal has significantly enhanced optical–electrical properties such as carrier mobility of 9.52 cm^2 V^{-1} s^{-1} and mobility-lifetime ($\mu\tau$) product of 2.9×10^{-4} cm^2 V^{-1}. The positive effect of Li^+-doped on the properties of $Cs_3Cu_2I_5$ crystal is approved by experiments and DFT calculation. The physical mechanism need to be studied further. The efficient direct X-ray detector composed of the $Cs_3Cu_2I_5$:Li single crystal (Au/$Cs_3Cu_2I_5$:Li/PCBM/Au) shows a high sensitivity of 831.1 μC Gy_{air}^{-1} cm^{-2}, low detection limit of 34.8 nGy_{air} s^{-1}, and excellent stability under continuous X-ray radiation. The results demonstrate the high potential of the $Cs_3Cu_2I_5$:Li single crystal in direct X-ray detection.

4. Experimental Section

Materials: Anhydrous 99.999% pure CuI (ALDRICH) and 99.99% pure CsI and LiI (APL Engineered Materials, Inc.) were used as starting materials. The pure and 2.5at.% Li^+-doped $Cs_3Cu_2I_5$ crystals were grown by the Bridgman method. Owing to the similar Shannon radii, Li^+ was assumed to substitute for Cu^+ (d^{10}). The mixture was charged into a quartz crucible with a straight capillary on the bottom. The crucible was evacuated to a pressure 5×10^{-5} Pa and sealed with an oxyhydrogen flame. The sealed ampoule was transferred to a three-zone Bridgman furnace and the temperature in the three-zone was 460, 480, and 200 °C, respectively. To completely melt the starting materials, the quartz crucible was held in the high-temperature zone for 40 h. The temperature gradient near the solid–liquid interface was 20 °C cm^{-1} and the quartz crucible was descended at a speed of 0.5–1 mm h^{-1}. Finally, the furnace cooled to room temperature in 60 h to obtain the $Cs_3Cu_2I_5$ single crystal.

Material Characterization: The crystal structure and phases were determined on the SmartLab SE X-ray diffractometer with Cu Kα radiation ($\lambda = 0.1541$ nm). Inductively coupled plasma optical emission spectrometry (ICP-OES) (Agilent Technologies 5100) and X-ray photoelectron spectroscopy (XPS) (Thermo Scientific K-Alpha) were carried out to determine the chemical composition. The electronic properties were evaluated by Hall-effects using the PPMS-9 comprehensive physical property measurement system as well as photoconduction measurements. The photoluminescence excitation (PLE) spectra, photoluminescence (PL) spectra, and decay time data were obtained on an FLS1000 spectrometer with a pulsed nano-LED under ultraviolet–visible (UV) light irradiation. The absorption spectra were acquired on the UV spectrophotometer (UV2600, SDPTOP).

Computation Details: The density functional theory computations were performed using the Vienna Ab-initio Simulation Package(VASP).[35–38] The hybrid exchange–correlation functional Perdew–Burke–Ernzerhof (PBE)[39] together with the projected augmented wave (PAW) potentials[40,41] was employed in the current calculations to better reproduce the band structures.[42] The total density of states (DOS) and projected DOS (PDOS) vacancy defects of Cs, Cu, Li, and I were calculated by the DFT-PBE level. The wavefunctions expanded in plane waves were cut off to a 550 eV kinetic energy and the Brillouin zone was sampled using a Γ-centered $2 \times 2 \times 2$ k-mesh, which was examined to have good convergence against denser k-points.

Detector Performance: The X-ray detection properties of the detector were evaluated using an X-ray generation system for medical imaging (Varex, G242, 18932-M8, USA) at an accelerating voltage of 50 kV and currents were ranging from 10 to 200 uA. The dose rate of the X-rays was calibrated with an X2 CT dosimeter (Unfors Raysafe, Sweden). During the measurement, the environment was kept dark and the external electrical bias and current were recorded by the PDA FS380 semiconductor analyzer. The X-ray imaging capability of the detector was demonstrated by moving the object between the detector (1 mm^2) and X-ray beam (1.62 mGy_{air} s^{-1}) using a self-assembled x–y scanning system consisting of a motorized linear displacement stage (Newport, M-IMS400CC. A motorized linear displacement stage combined with a motion controller (Newport, M-IMS400CC) was used to control scanning along the x and y axes.

Supporting Information

Supporting Information is available from the Wiley Online Library or from the author.

Acknowledgements

Q.W. and X.F. contributed equally to this work.The authors acknowledge the financial support provided by the National Natural Science Foundation of China (NSFC) (no. 12275262, 21975280, 62004091, and 12235006), the Natural Science Foundation of Zhejiang (no. Z23E020002 and LGG22E020001), the Shenzhen Excellent Science and Technology Innovation Talent Training Project-Outstanding Youth Project (RCJC20200714114435061), the Shenzhen Basic Research Program (JCYJ20200109115212546), the Chinese Academy of Sciences Special Research Assistant Project (Y95909), and the Chinese Academy of Sciences Excellent Youth Innovation Fund grade B (E2G0161001). The City University of Hong Kong Donation Research Grant (DON-RMG 9229021), the City University of Hong Kong Donation Grant (9220061), the Hong Kong PDFS – RGC Postdoctoral Fellowship Scheme (PDFS2122-1S08 and CityU 9061014), as well as Hong Kong HMRF (Health and Medical Research Fund) (2120972 and CityU 9211320) are acknowledged. The authors also acknowledge Professor Jiang Tang of Huazhong University of Science and Technology for his useful advice.

Conflict of Interest

The authors declare no conflict of interest.

Data Availability Statement

The data that support the findings of this study are available on request from the corresponding author. The data are not publicly available due to privacy or ethical restrictions.

Keywords

copper-based halides, $Cs_3Cu_2I_5$:Li single crystal, direct X-ray detection, semiconductors

Received: February 1, 2023
Revised: May 5, 2023
Published online: June 28, 2023

[1] X. Ou, X. Chen, X. Xu, L. Xie, X. Chen, Z. Hong, H. Bai, X. Liu, Q. Chen, L. Li, H. Yang, *Research* **2021**, *2021*, 9892152.
[2] S. M. Lee, J. B. Seo, J. Yun, Y.-H. Cho, J. Vogel-Claussen, M. L. Schiebler, W. B. Gefter, E. J. R. van Beek, J. M. Goo, K. S. Lee, H. Hatabu, J. Gee, N. Kim, *J. Thorac. Imaging* **2019**, *34*, 75.
[3] X. Mei, H. C. Lee, K. Y. Diao, M. Huang, B. Lin, C. Liu, Z. Xie, Y. Ma, P. M. Robson, M. Chung, A. Bernheim, V. Mani, C. Calcagno, K. Li, S. Li, H. Shan, J. Lv, T. Zhao, J. Xia, Q. Long, S. Steinberger, A. Jacobi, T. Deyer, M. Luksza, F. Liu, B. P. Little, Z. A. Fayad, Y. Yang, *Nat. Med.* **2020**, *26*, 1224.
[4] H. Wu, Y. Ge, G. Niu, J. Tang, *Matter* **2021**, *4*, 144.
[5] Z. George, D. P. Larry, P. Raisa, P. Cesar, F. V. Gary, N. B. Barry, I. V. Alexander, D. Ofer, E. Meerson, M. Schieber, G. Haim, A. T. Jerry, *Proc. SPIE* **2003**, *5030*, 77
[6] R. Wu, D. FAN, Y. Kang, X. Wan, C. Guo, D. Wei, D. Chen, T. WANG, *J. Synth. Cryst.* **2021**, *50*, 1813.
[7] M. Guerra, M. Manso, S. Longelin, S. Pessanha, M. L. Carvalho, *J. Instrum.* **2012**, *7*, C10004.
[8] S. O. Kasap, *J. Phys. D: Appl. Phys.* **2000**, *33*, 2853.
[9] M. Schieber, H. Hermon, A. Zuck, A. Vilensky, L. Melekhov, R. Shatunovsky, E. Meerson, Y. Saado, M. Lukach, E. Pinkhasy, S. E. Ready, R. A. Street, *J. Cryst. Growth* **2001**, *225*, 118.
[10] C. Szeles, *Phys. Status Solidi B.* **2004**, *241*, 783.
[11] Y. Zhou, J. Chen, O. M. Bakr, O. F. Mohammed, *ACS Energy Lett.* **2021**, *6*, 739.
[12] S. Wang, F. Yang, J. Zhu, Q. Cao, Y. Zhong, A. Wang, W. Du, X. Liu, *Sci. China Mater.* **2020**, *63*, 1438.
[13] Y. Su, W. Ma, Y. Yang, *J. Semicond.* **2020**, *41*, 051204.
[14] H. Wei, J. Huang, *Nat. Commun.* **2019**, *10*, 1066.
[15] W. Liang, Z. Shi, Y. Li, J. Ma, S. Yin, X. Chen, D. Wu, Y. Tian, Y. Tian, Y. Zhang, X. Li, C. Shan, *ACS Appl. Mater. Interfaces* **2020**, *12*, 37363.
[16] S. Fang, Y. Wang, H. Li, F. Fang, K. Jiang, Z. Liu, H. Li, Y. Shi, *J. Mater. Chem. C* **2020**, *8*, 4895.
[17] T. Jun, K. Sim, S. Iimura, M. Sasase, H. Kamioka, J. Kim, H. Hosono, *Adv. Mater.* **2018**, *30*, 1804547.
[18] S. Cheng, A. Beitlerova, R. Kucerkova, M. Nikl, G. Ren, Y. Wu, *Phys. Status Solidi RRL* **2020**, *14*, 2000374.
[19] D. Liu, Q. Wei, Y. Tong, P. Xiang, P. Cai, G. Tang, H. Shi, L. Qin, *CrystEngComm* **2023**, *25*, 58.
[20] J. Zhou, K. An, P. He, J. Yang, C. Zhou, Y. Luo, W. Kang, W. Hu, P. Feng, M. Zhou, X. Tang, *Adv. Opt. Mater.* **2021**, *9*, 2002144.
[21] D. Yuan, *ACS Appl. Mater. Interfaces* **2020**, *12*, 38333.
[22] S. Cheng, M. Nikl, A. Beitlerova, R. Kucerkova, X. Du, G. Niu, Y. Jia, J. Tang, G. Ren, Y. Wu, *Adv. Opt. Mater.* **2021**, *9*, 2100460.
[23] P. Xiang, Q. Wei, C. Wang, P. Cai, Y. Tong, G. Tang, X. Sun, F. Yang, H. Shi, Z. Liu, L. Qin, *J. Mater. Chem. C* **2022**, *10*, 15400.
[24] Q. Wang, Q. Zhou, M. Nikl, J. Xiao, R. Kucerkova, A. Beitlerova, V. Babin, P. Prusa, V. Linhart, J. Wang, X. Wen, G. Niu, J. Tang, G. Ren, Y. Wu, *Adv. Opt. Mater.* **2022**, *10*, 2200304.
[25] L. Lian, M. Zheng, W. Zhang, L. Yin, X. Du, P. Zhang, X. Zhang, J. Gao, D. Zhang, L. Gao, *Adv. Sci.* **2020**, *7*, 2000195.
[26] Y. Liu, Z. Xu, Z. Yang, Y. Zhang, J. Cui, Y. He, H. Ye, K. Zhao, H. Sun, R. Lu, M. Liu, M. Kanatzidis, S. L. Frank Liu, *Matter* **2020**, *3*, 180.
[27] C. Foster, Y. Wu, M. Koschan, C. L. Melcher, *Phys. Status Solidi RRL* **2018**, *12*, 1800280.
[28] P. Cheng, L. Sun, L. Feng, S. Yang, Y. Yang, D. Zheng, Y. Zhao, Y. Sang, R. Zhang, D. Wei, W. Deng, K. Han, *Angew. Chem., Int. Ed.* **2019**, *58*, 16087.
[29] J. Tauc, A. Menth, *J. Non-Cryst. Solids* **1972**, *569*, 8.
[30] D. McGregor, H. Hermon, *Nucl. Instrum. Methods Phys. Res., Sect. A* **1997**, *395*, 101.
[31] X. Li, P. Zhang, Y. Hua, F. Cui, X. Sun, L. Liu, Y. Bi, Z. Yue, G. Zhang, X. Tao, *ACS Appl. Mater. Interfaces* **2022**, *14*, 9340.
[32] W. Pan, H. Wu, J. Luo, Z. Deng, C. Ge, C. Chen, X. Jiang, W.-J. Yin, G. Niu, L. Zhu, L. Yin, Y. Zhou, Q. Xie, X. Ke, M. Sui, J. Tang, *Nat. Photonics* **2017**, *11*, 726.
[33] L. Li, X. Liu, H. Zhang, B. Zhang, W. Jie, P. J. Sellin, C. Hu, G. Zeng, Y. Xu, *ACS Appl. Mater. Interfaces* **2019**, *11*, 7522.
[34] M. J. Berger, J. H. Hubbell, S. M. Seltzer, J. Chang, J. S. Coursey, R. Sukumar, D. S. Zucker, K. Olsen, XCOM: photon cross sections database NIST http://physics.nist.gov/xcom (accessed: November **2010**).
[35] G. Kresse, J. Hafner, *Phys. Rev. B* **1993**, *47*, 558.
[36] G. Kresse, J. Hafner, *Phys. Rev. B* **1994**, *49*, 14251.
[37] G. Kresse, J. Furthmüller, *Comp. Mater. Sci.* **1996**, *6*, 15.
[38] G. Kresse, J. Furthmüller, *Phys. Rev. B* **1996**, *54*, 11169.
[39] J. P. Perdew, K. Burke, M. Ernzerhof, *Phys. Rev. Lett.* **1996**, *77*, 3865.
[40] P. E. Blöchl, *Phys. Rev. B* **1994**, *50*, 17953.
[41] G. Kresse, D. Joubert, *Phys. Rev. B* **1999**, *59*, 1758.
[42] J. Paier, R. Hirschl, M. Marsman, G. Kresse, *J. Chem. Phys.* **2005**, *122*, 234102.

ADVANCED OPTICAL MATERIALS

Supporting Information

for *Adv. Optical Mater.*, DOI 10.1002/adom.202300247

$Cs_3Cu_2I_5$ Single Crystal for Efficient Direct X-Ray Detection

Qinhua Wei, Xiongsheng Fan, Peng Xiang, Laishun Qin, Wenjun Liu, Tongyu Shi, Hang Yin, Peiqing Cai, Yufeng Tong, Gao Tang, Zugang Liu, Paul K. Chu, Hongsheng Shi*, Yanliang Liu* and Xue-Feng Yu**

Supporting Information

$Cs_3Cu_2I_5$ Single Crystal for Efficient Direct X-ray Detection

Qinhua Wei[a§], Xiongsheng Fan[b,c§], Peng Xiang[a], Laishun Qin[a*], Wenjun Liu[b], Tongyu Shi[b], Hang Yin[a,d], Peiqing Cai[c], Yufeng Tong[a], Gao Tang[a], Zugang Liu[c], Paul K. Chu[f], Hongsheng Shi[e*], Yanliang Liu [b*] and Xue-Feng Yu [b*]

[a] College of Materials and Chemistry, China Jiliang University, Hangzhou 310018, China

[b] Shenzhen Institute of Advanced Technology, Chinese Academy of Sciences, Shenzhen 518055, Guangdong, China

[c] College of Optical and Electronic Technology, China Jiliang University, Hangzhou 310018, China

[d] State Key Laboratory of Molecular Reaction Dynamics, Dalian Institute of Chemical Physics, Chinese Academy of Science, Dalian 116023, China.

[e] Xinjiang Technical Institute of Physics and Chemistry, Chinese Academy of Sciences, Urumqi 830011

[f] Department of Physics, Department of Materials Science and Engineering, and Department of Biomedical Engineering, City University of Hong Kong, Tat Chee Avenue, Kowloon, Hong Kong, China

[§] These authors contributed equally to this work.

[*] Corresponding authors: Emails: qinlaishun@cjlu.edu.cn (Laishun Qin); shs1975@126.com (Hongsheng Shi); xf.yu@siat.ac.cn (Xue-Feng Yu), yl.liu4@siat.ac.cn (Yanliang Liu)

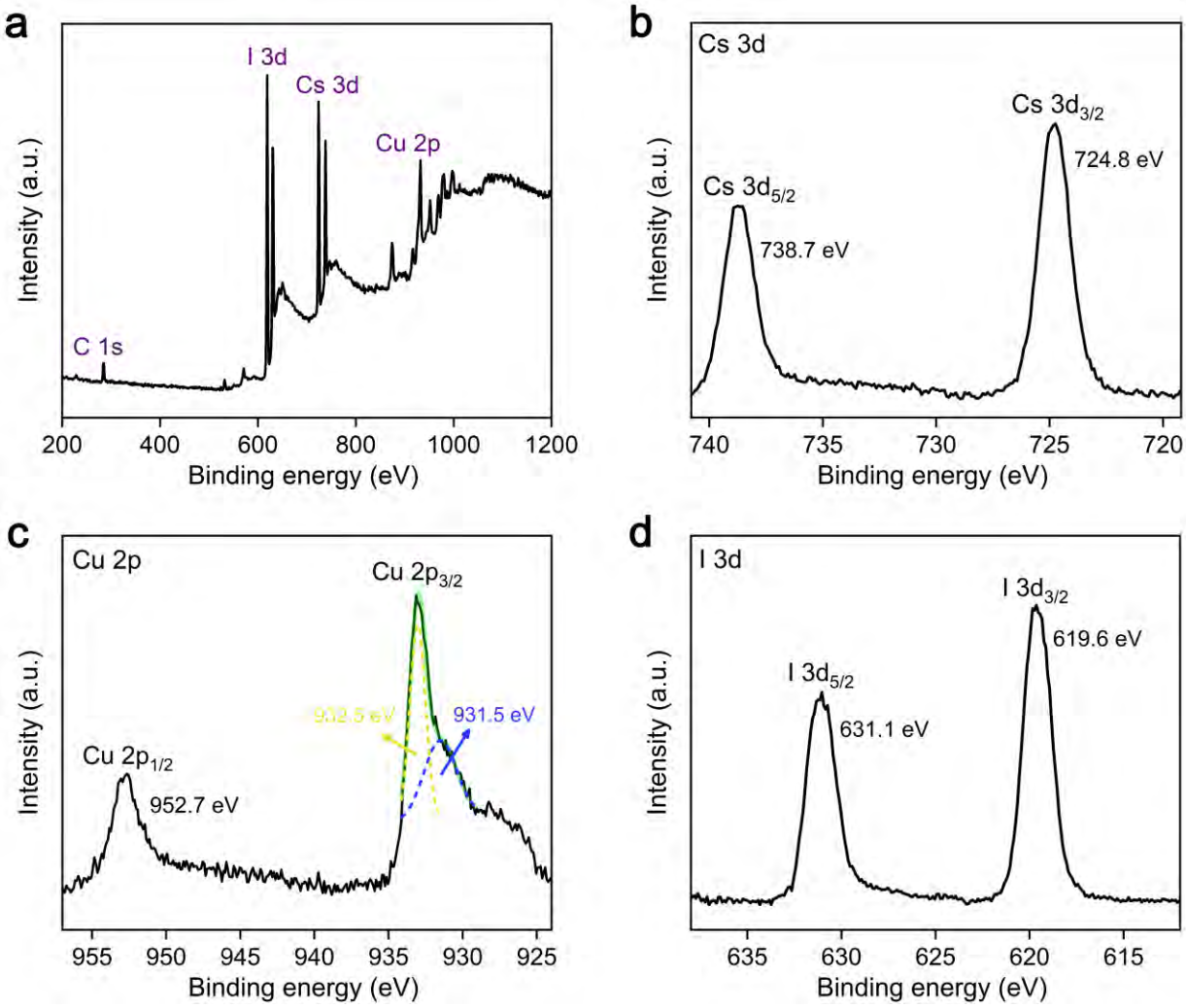

Figure S1. XPS survey spectrum of $Cs_3Cu_2I_5$ crystal.

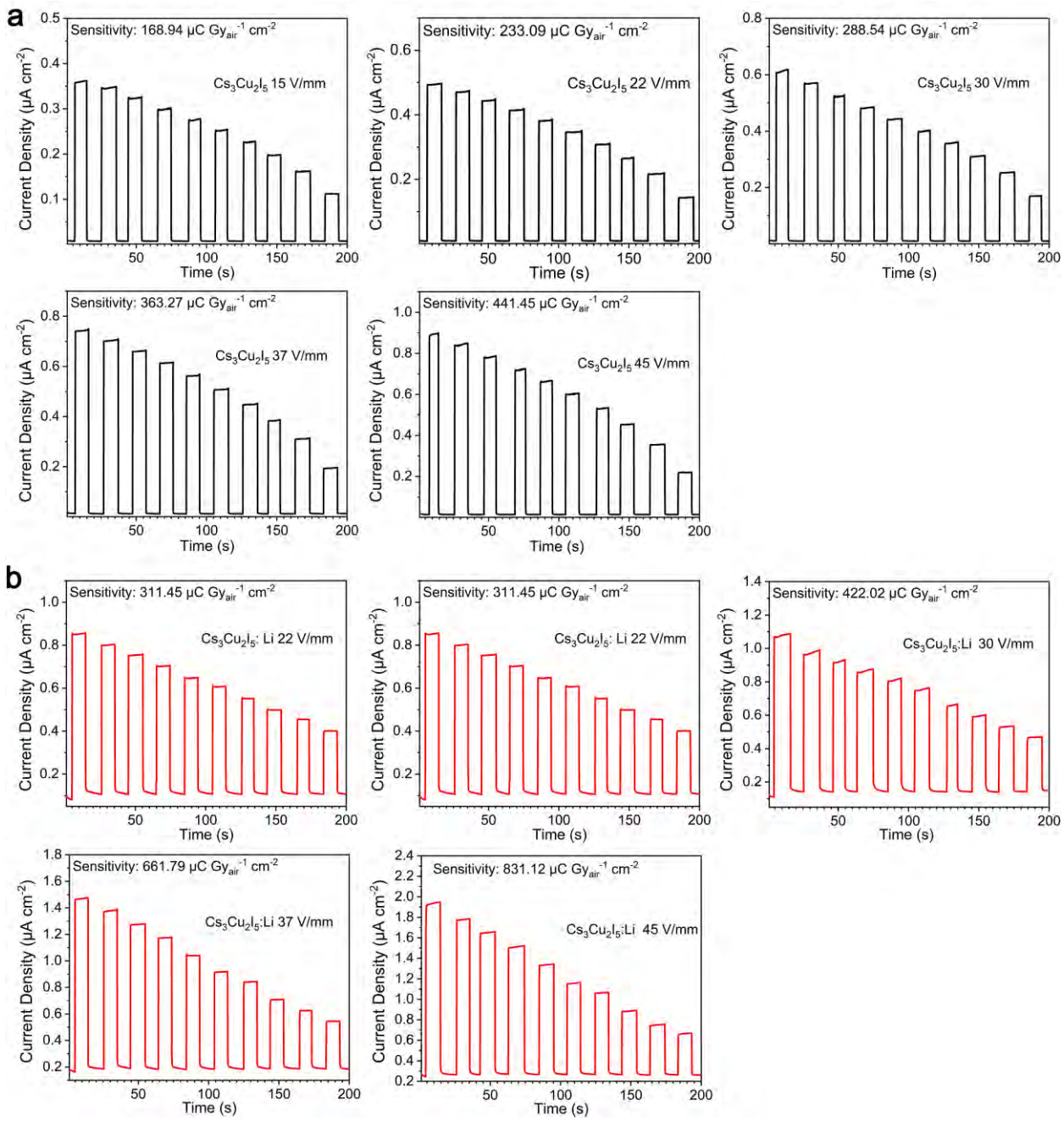

Figure S2. The current response upon X-ray on/off for the (a) $Cs_3Cu_2I_5$ and (b) $Cs_3Cu_2I_5$:Li detectors at different electric fields and various X-ray dose rates

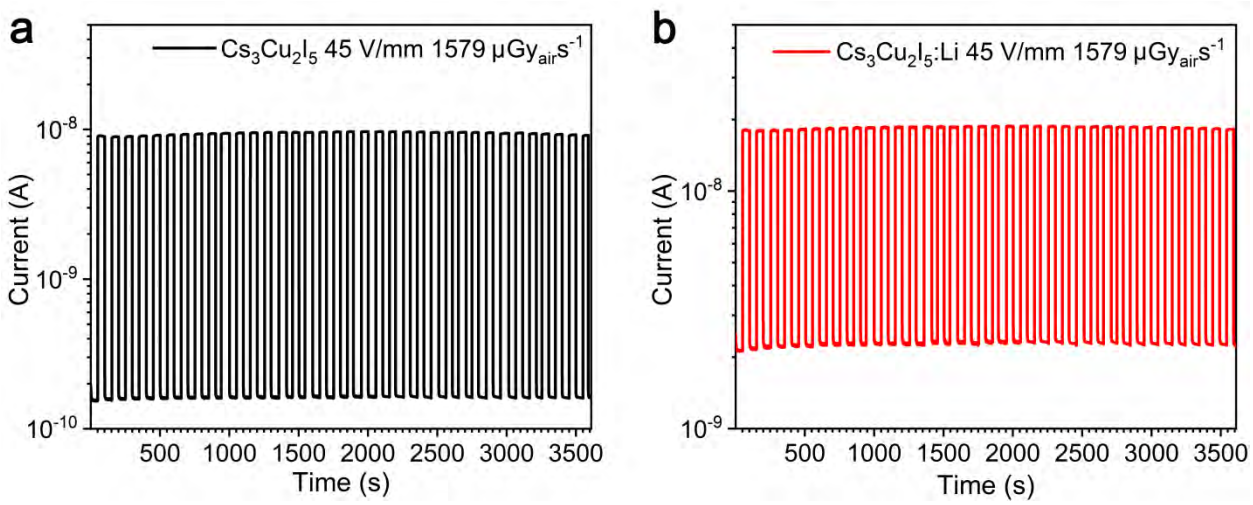

Figure S3. The X-ray on/off experiments of the (a) $Cs_3Cu_2I_5$ and (b) $Cs_3Cu_2I_5$:Li detectors under 45 V/mm external electric field and 1579 $\mu Gy_{air}\ s^{-1}$ X-ray dose for 3600 s

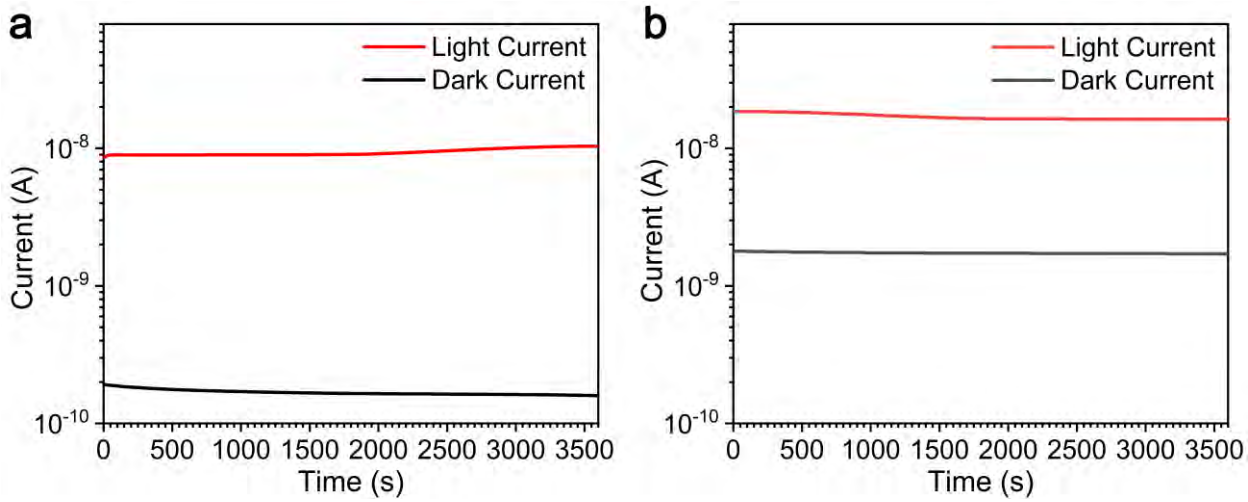

Figure S4. The temporal baseline tracking of the (a) $Cs_3Cu_2I_5$ and (b) $Cs_3Cu_2I_5$:Li detectors

Table S1. Characteristic parameters of various direct perovskite detectors.

Materials (Single crystal)	μτ product ($cm^2 V^{-1}$)	Sensitivity ($\mu C Gy^{-1} cm^{-2}$)	Detection limit ($nGy s^{-1}$)	Resistivity (Ω cm)	electric field ($V mm^{-1}$)	Ref
$MAPbBr_3$	1.2×10^{-2}	80	500	1.7×10^{7}		[1]
$MAPbBr_3$	2.6×10^{-4}	529	1210	1.26×10^{8}	5	[2]
$CsPbBr_3$	2.5×10^{-3}	1256		7.85×10^{9}	20	[3]
$(F\text{-}PEA)_2PbI_4$	5.1×10^{-4}	3402	23	1.36×10^{12}	133.3	[4]
$Cs_2AgBiBr_6$	6.3×10^{-3}	105	59.7	1.6×10^{11}	25	[5]
$Cs_2AgBiBr_6$	5.95×10^{-3}	1974	45.7	3.31×10^{10}	50	[6]
$Cs_3Bi_2I_9$	7.97×10^{-4}	1652.3	130	2.79×10^{10}	50	[7]
$Rb_3Bi_2I_9$	2.51×10^{-3}	159.7	8.32	2.3×10^{11}	300	[8]
$MA_3Bi_2I_9$	2.87×10^{-3}	1947	83	3.74×10^{10}	60	[9]
$MA_3Bi_2I_9$	2.8×10^{-3}	10620	0.62	5.27×10^{-3}	48	[10]
$Cs_3Cu_2I_5$	1.4×10^{-4}	441.5	335.1	4.3×10^{11}	45	This work
$Cs_3Cu_2I_5$:Li	2.9×10^{-4}	831.1	34.8	2.7×10^{10}	45	This work

References

[1] H. Wei, Y. Fang, P. Mulligan, W. Chuirazzi, H. H. Fang, C. Wang, B. R. Ecker, Y. Gao, M. A. Loi, L. Cao, *Nat. Photonics* **2016**, 10, 333.

[2] L. Li, X. Liu, H. Zhang, B. Zhang, W. Jie, P. J. Sellin, C. Hu, G. Zeng, Y. Xu, *ACS Appl. Mater. Interfaces* **2019**, 11, 7522.

[3] H. Zhang, F. Wang, Y. Lu, Q. Sun, Y. Xu, B.-B. Zhang, W. Jie, M. G. Kanatzidis, *J. Mater. Chem. C* **2020**, 8, 1248.

[4] H. Li, J. Song, W. Pan, D. Xu, W.-a. Zhu, H. Wei, B. Yang, *Adv. Mater.* **2020**, 32, 2003790.

[5] W. Pan, H. Wu, J. Luo, Z. Deng, C. Ge, C. Chen, X. Jiang, W.-J. Yin, G. Niu, L. Zhu, L. Yin, Y. Zhou, Q. Xie, X. Ke, M. Sui, J. Tang, *Nat. Photonics* **2017**, 11, 726.

[6] L. Yin, H. Wu, W. Pan, B. Yang, P. Li, J. Luo, G. Niu, J. Tang, *Adv. Opt. Mater.* **2019**, 7, 1900491.

[7] Y. Zhang, Y. Liu, Z. Xu, H. Ye, Z. Yang, J. You, M. Liu, Y. He, M. G. Kanatzidis, S. Liu, *Nat. Commun.* **2020**, 11, 2304.

[8] M. Xia, J. H. Yuan, G. Niu, X. Du, L. Yin, W. Pan, J. Luo, Z. Li, H. Zhao, K. H. Xue, *Adv. Funct. Mater.* **2020**, 30, 1910648.

[9] Y. Liu, Z. Xu, Z. Yang, Y. Zhang, J. Cui, Y. He, H. Ye, K. Zhao, H. Sun, R. Lu, M. Liu, M. Kanatzidis, S. L. Frank Liu, *Matter* **2020**, 3, 180.

[10] X. Zheng, W. Zhao, P. Wang, H. Tan, M. I. Saidaminov, S. Tie, L. Chen, Y. Peng, J. Long, W.-H. Zhang, *J. Energy Chem.* **2020**, 49, 299.